

---

# SPAE: Semantic Pyramid AutoEncoder for Multimodal Generation with Frozen LLMs

---

Lijun Yu<sup>††\*</sup> Yong Cheng<sup>†</sup> Zhiruo Wang<sup>‡</sup> Vivek Kumar<sup>†</sup> Wolfgang Macherey<sup>†</sup>  
Yanping Huang<sup>†</sup> David A. Ross<sup>†</sup> Irfan Essa<sup>†</sup> Yonatan Bisk<sup>‡</sup> Ming-Hsuan Yang<sup>†</sup>  
Kevin Murphy<sup>†</sup> Alexander G. Hauptmann<sup>‡</sup> Lu Jiang<sup>†‡</sup>

<sup>†</sup>Google, <sup>‡</sup>Carnegie Mellon University

## Abstract

In this work, we introduce Semantic Pyramid AutoEncoder (SPAE) for enabling frozen LLMs to perform both understanding and generation tasks involving non-linguistic modalities such as images or videos. SPAE converts between raw pixels and interpretable lexical tokens (or words) extracted from the LLM’s vocabulary. The resulting tokens capture both the semantic meaning and the fine-grained details needed for visual reconstruction, effectively translating the visual content into a language comprehensible to the LLM, and empowering it to perform a wide array of multimodal tasks. Our approach is validated through in-context learning experiments with frozen PaLM 2 and GPT 3.5 on a diverse set of image understanding and generation tasks. Our method marks the first successful attempt to enable a frozen LLM to generate image content while surpassing state-of-the-art performance in image understanding tasks, under the same setting, by over 25%.

## 1 Introduction

Large language models (LLMs) empowered by Transformers [38] have achieved remarkable progress in addressing a broad spectrum of Natural Language Processing (NLP) tasks [4, 8, 28, 2]. With the continuous increases in model size and training data, LLMs are gradually becoming more versatile and agnostic to specific tasks, unlocking new capabilities in solving complex AI tasks [42], like question answering, code generation, reasoning, mathematics problem-solving, and understanding humor, among various other applications [2, 28].

LLMs capture rich conceptual knowledge about the world in their lexical embeddings. This raises a question: if provided with the appropriate visual representations as input, *are frozen LLMs capable of solving tasks in visual modalities?* Very recently, there have been notable advancements in extending the capabilities of frozen LLMs to tackle image understanding and retrieval tasks [21, 27]. However, generating a different modality using a frozen LLM that has not been explicitly trained on that modality has proven to be challenging and has had little success.

To facilitate LLMs for such cross-modal tasks, we propose to learn a vector quantizer to map an image, or some other non-linguistic (“foreign”) modality, to the token space of a frozen LLM. This effectively translates the image into a language that the LLM can comprehend, enabling us to leverage the generative abilities of the LLM to perform image understanding and generation tasks without having to train on image-text pairs. Specifically, our new approach is that, given an image prompt, convert it to a token space with our learned encoder, use the LLM to generate suitable lexical tokens, and convert back to pixel space with our learned decoder.

---

\*Work partially done during a research internship at Google Research.

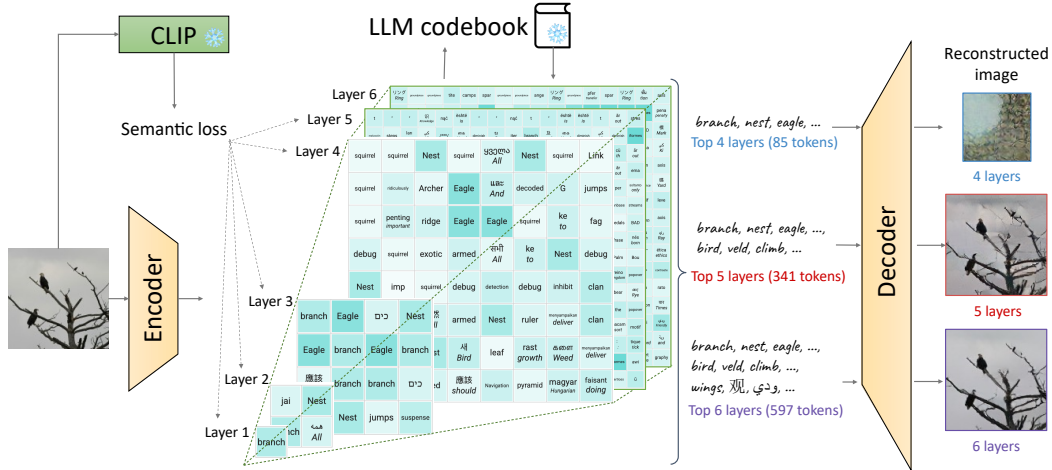


Figure 1. **Framework of the proposed SPAE model.** An image is encoded into a pyramid of lexical tokens capturing semantic concepts and appearance details necessary for reconstruction.

We introduce a novel Semantic Pyramid AutoEncoder (SPAE) that produces a lexical word sequence that (1) carries rich semantics, and (2) retains fine details for signal reconstruction. In contrast to the majority of VQ-VAE approaches [37], our encoder maps to an interpretable discrete latent space, *i.e.*, words. As depicted in Fig. 1, SPAE tokens have a multi-scale representation arranged in a pyramid structure. The upper layers of the pyramid comprise semantic-central concepts, while the lower layers prioritize appearance representations that captures the fine details for image reconstruction. This design enables us to dynamically adjust the token length to accommodate various tasks, such as using fewer tokens for understanding tasks and more tokens for generation tasks.

We verify the plausibility of our approach in an extreme setting of in-context learning [4], without any parameter updates to the LLM. Our SPAE model is trained standalone, without backpropagating through any language model. We evaluate our approach on image understanding tasks including image classification, image captioning, and visual question answering. We showcase a promising direction to image generation with LLMs by utilizing in-context denoising techniques. Our method is LLM-agnostic and has been tested with PaLM 2 [2] and GPT-3.5 [28], suggesting compatibility with arbitrary LLMs.

The main contributions of this work are summarized as follows:

- This is the first successful method, to the best of our knowledge, that uses a frozen language model, trained solely on language tokens, to directly generate image content through in-context learning.
- We introduce a new SPAE tokenizer producing interpretable representations of semantic concepts and fine-grained details in the form of multilingual linguistic tokens with adjustable lengths.
- We evaluate our method on visual understanding and generation tasks, and notably, our approach outperforms the best-published few-shot image classification accuracy [27] by an absolute 25% under the same in-context setting.

## 2 Related Work

**Multimodal generation with LLMs.** Advances have been made to expand the capabilities of LLMs beyond language. For example, Visual ChatGPT [43] uses ChatGPT to generate prompts and executes multimodal tasks through another model, *e.g.*, generating image from text prompts by Stable Diffusion [32]. FROMAGe [21] feeds CLIP [30] embeddings to OPT [49] for image understanding and retrieval. However, it requires backpropagation through the LLM and does not support image synthesis. This work enables a standalone frozen LLM to understand and generate other modalities which are unseen in training.

**Tokenization via vector quantization.** VQ-VAE [37] compresses data into a discrete latent space defined by a codebook via vector quantization. VQGAN [14] enhances the reconstruction quality with adversarial and perceptual objectives. These discrete latent quantities, often referred to as *tokens*, are widely used to learn generative transformer models for image [32, 7], video [45, 15, 39], image-video [46], and audio [3, 9]. Our SPAE model is built upon the VQGAN framework and applicable to different modalities.

**Tokenization into lexical representations.** The codebooks in typical VQGANs are learned jointly with the encoder and decoder stacks, which are not directly interpretable via natural languages. LQAE [27] replaces the learned codebook with frozen word embeddings from BERT [12] to connect with an English vocabulary. However, the LQAE tokens seldom contain semantic concepts in an image, and the reconstruction quality is worse than that with a learned codebook. Our SPAE quantizes an input sample into semantically related tokens in a multilingual vocabulary while preserving the high reconstruction quality of a VQGAN for generative tasks. In addition, SPAE tokens are organized in a multi-layer coarse-to-fine pyramid for flexible usage in different tasks.

**Few-shot learning with LLMs.** In-context learning [4, 8, 2] facilitates LLMs for few-shot learning via the text interface without parameter updates. This approach is commonly employed to assess the performance of LLMs on numerous NLP benchmarks, *e.g.*, classification and question answering [41], mathematical reasoning [24], and code generation [44], which yields competitive results to their fine-tuned counterparts. However, existing few-shot vision-language understanding and generation frameworks [1, 21] still require LLM parameter updates. In contrast, our work inherits the in-context learning ability from frozen LLMs.

### 3 Method

Our goal is to model an image, or some other non-linguistic modality (*e.g.*, video or audio), as a language sequence that LLMs can comprehend. *Semantic Pyramid AutoEncoder* (SPAE) generates a lexical word sequence with dynamically adjustable length that carries rich semantics and retains fine details for signal reconstruction. To work with a frozen LLM via in-context learning, we introduce a progressive in-context denoising method to facilitate image generation. We use the image modality in this section to introduce our SPAE model in 2D, and later showcase the results of a 3D variant with the video modality in our experiments.

#### 3.1 Semantic Pyramid AutoEncoder

Our SPAE model extends the VQ-VAE [37] framework, which comprises an encoder, a quantizer, and a decoder. The CNN encoder maps an image  $\mathbf{I} \in \mathbb{R}^{H \times W \times 3}$  into continuous embeddings  $\mathbf{Z} \in \mathbb{R}^{h \times w \times c}$ . Each element  $\mathbf{z} \in \mathbf{Z}$  is then passed through the quantizer, which assigns it to the closest entry in a codebook, resulting in the quantized embedding. Let  $\hat{\mathbf{Z}}$  represent the quantized embeddings for the entire image. The CNN decoder receives  $\hat{\mathbf{Z}}$  as input and generates the reconstructed image  $\hat{\mathbf{I}}$ . Below we highlight the design differences in SPAE.

As illustrated in Fig. 1, SPAE generates lexical tokens arranged in a pyramid structure, which contains semantic concepts in the upper layers and appearance with progressively refined details in the lower layers. We introduce a semantic loss to encourage the usage of conceptually relevant tokens.

**Frozen language codebook.** To generate lexical tokens, we utilize a pretrained LLM codebook  $\mathbb{C} = \{(k, \mathbf{e}(k)) \mid k \in \mathbb{T}\}$  and freeze it during training, where  $\mathbb{T}$  is a subset of the LLM vocabulary. Here,  $\mathbf{e}(\cdot)$  produces the text embedding for a sub-word  $k$  which may be obtained from any layer of the LLM. Since the codebook is aligned with the language vocabulary, we use the terms “token” and “word” interchangeably.

**Token pyramid.** The SPAE quantizer produces  $D$  layers of tokens where the tokens at layer  $l$  are denoted as  $\mathbf{k}_l \in \mathbb{T}^{h_l \times w_l}$ . Prior works use Residual Quantization (RQ) to generate multi-layer tokens [22, 47]. In these methods, tokens from all layers have uniform shapes and do not carry specific semantic meanings. In contrast, we propose a pyramid token structure by enforcing the constraint  $h_l \leq h_{l+1} \wedge w_l \leq w_{l+1}$ . The pyramid structure is purposefully designed to concentrate semantics within the within the upper layers of the pyramid. This design allows for representing semantic concepts with notably fewer tokens, *e.g.*, as few as five tokens for understanding tasks. The high token efficiency stems from the pyramid structure, as a conventional layer without pyramid structures needs a minimum of  $hw$  tokens (*e.g.*, 256) to represent the image. Token efficiency is crucial for in-context learning as it enables the accommodation of more examples within the context. A dilation subsampler  $\mathbf{P}(l)$  is used, which selects the positions for quantization at layer  $l$  as

$$\mathbf{P}(l) = \{(h' i - \lfloor \frac{h'}{2} \rfloor + 1, w' j - \lfloor \frac{w'}{2} \rfloor + 1) \mid (i, j) \in ([1, h_l] \times [1, w_l]) \cap \mathbb{Z}^2\}, \quad (1)$$

where  $h' = \frac{h_D}{h_l}$ , and  $w' = \frac{w_D}{w_l}$  are the downsample ratios.

For each embedding  $\mathbf{z}$  at position  $(x, y)$ , we obtain its discrete tokens sequentially from layer 1 to  $D$ . At layer  $l$ , if  $(x, y) \in \mathbf{P}(l)$ , the quantizer assigns discrete token  $k_l = \arg \min_{k \in \mathbb{T}} \|\mathbf{z}_l - \mathbf{e}(k)\|_2^2$ ,

where  $\mathbf{z}_l$  is the current layer embedding, calculated from

$$\mathbf{z}_l = \mathbf{z} + \sum_{i=1}^{l-1} \mathbf{1}_{(x,y) \in \mathbf{P}(i)} (\mathbf{z} - \mathbf{e}(k_i)). \quad (2)$$

The quantized embedding reconstructed with the first  $l$  layers is given by the average of the existing token embeddings as

$$\hat{\mathbf{z}}_{\leq l} = \frac{\sum_{i=1}^l \mathbf{1}_{(x,y) \in \mathbf{P}(i)} \mathbf{e}(k_i)}{\sum_{i=1}^l \mathbf{1}_{(x,y) \in \mathbf{P}(i)}}. \quad (3)$$

Using the input of  $\hat{\mathbf{Z}}_{\leq l}$  from tokens up to layer  $l$ , the decoder can progressively reconstruct the image with dynamic token lengths, resulting in gradually improved quality with refined appearance details. We term this approach as *Streaming Average Quantization* (SAQ) due to its resemblance to computing the average on streaming data, where  $\hat{\mathbf{z}}_{\leq l+1} = \hat{\mathbf{z}}_{\leq l} + \frac{1}{l+1} \mathbf{e}(k_{l+1})$ ,  $\hat{l} = \sum_{i=1}^l \mathbf{1}_{(x,y) \in \mathbf{P}(i)}$ .

RQ [22, 47] is applicable but yields worse results in this context, as revealed by our ablation studies. This can be attributed to (1) varying scales of embeddings in residual layers, potentially dividing the codebook into multiple parts, and (2) misalignment in the summation of word embeddings, which undermines learning semantically meaningful tokens in later layers.

**Semantic loss.** We encourage the semantic similarity between the image  $\mathbf{I}$  and each lexical token  $k$  denoted by  $s(\mathbf{I}, k)$ . During training, we build per-layer candidate token pools as

$$\mathbf{C}_l(\mathbf{I}) = \{k \in \mathbb{T} \mid s(\mathbf{I}, k) \geq \rho_l\}, \quad (4)$$

where  $\rho_l$  is a threshold. We set  $\rho_l \geq \rho_{l+1}$  to allow deeper layers to have a larger pool of candidate tokens while sacrificing some semantics.

To define the similarity score, this paper employs a pretrained CLIP model [29]. In more details, let  $f_{\mathcal{I}}$  and  $f_{\mathcal{T}}$  be a pair of image and text CLIP embedding functions. We precompute the text feature for each token  $k \in \mathbb{T}$  as

$$f'_{\mathcal{T}}(k) = \frac{1}{|\mathbf{p}|} \sum_{i=1}^{|\mathbf{p}|} f_{\mathcal{T}}(\mathbf{p}_i(k)), \quad (5)$$

where  $\mathbf{p}$  is a list of prompt templates, such as "a photo of . . .". During training, we extract the image feature  $f_{\mathcal{I}}(\mathbf{I})$  and compute the dot-product similarity as  $s'(\mathbf{I}, k) = f_{\mathcal{I}}(\mathbf{I}) \cdot f'_{\mathcal{T}}(k)$ . The similarity score is then normalized to account for the varying scales across different images.

$$s(\mathbf{I}, k) = \frac{s'(\mathbf{I}, k) - \min_j s'(\mathbf{I}, j)}{\max_j s'(\mathbf{I}, j) - \min_j s'(\mathbf{I}, j)}. \quad (6)$$

We define the semantic loss for the encoder parameters  $\theta_e$  as

$$\mathcal{L}_{\text{semantic}}(\theta_e; \mathbf{I}) = \mathbb{E}_{l \in [1, D']} \mathbb{E}_{\mathbf{z}_l} \mathbb{E}_{c \in \mathbf{C}_l(\mathbf{I})} - \log \frac{\exp(-\|\mathbf{z}_l - \mathbf{e}(c)\|_2^2)}{\sum_{k \in \mathbb{T}} \exp(-\|\mathbf{z}_l - \mathbf{e}(k)\|_2^2)}, \quad (7)$$

where we randomly sample semantically similar target codes  $c$  for each layer embedding in the first  $D'$  layers.

**Appearance loss.** Using an improved objective from [45], the appearance loss is calculated as:

$$\mathcal{L}_{\text{appearance}}(\theta_e, \theta_d; \mathbf{I}) = \|\mathbf{I} - \hat{\mathbf{I}}\|_2^2 + \beta \sum_{l=1}^D \|\mathbf{Z} - \text{sg}(\hat{\mathbf{Z}}_{\leq l})\|_2^2 + \lambda \mathcal{L}_{\text{GAN}} + \eta \mathcal{L}_{\text{Perceptual}} + \phi \mathcal{L}_{\text{LeCAM}}, \quad (8)$$

where  $\mathcal{L}_{\text{GAN}}$ ,  $\mathcal{L}_{\text{Perceptual}}$ , and  $\mathcal{L}_{\text{LeCAM}}$  are the VQGAN [15], perceptual [19], and LeCAM [34] losses. In addition,  $\text{sg}(x)$  is the stop-gradient operation. The appearance loss is applied to both the encoder  $\theta_e$  and decoder parameters  $\theta_d$ , excluding the frozen codebook embedding.

To stabilize the training and balance between appearance and semantics, we add a dynamic weight for the semantic guidance loss as  $w = \text{sg}\left(\frac{\mathcal{L}_{\text{appearance}}(\mathbf{I})}{\mathcal{L}_{\text{semantic}}(\mathbf{I})}\right)$ . The total training loss excluding the GAN discriminator is

$$\mathcal{L}_{\text{SPAe}}(\theta_e, \theta_q) = \mathbb{E}_{\mathbf{I}} \left[ \mathcal{L}_{\text{appearance}}(\theta_e, \theta_q; \mathbf{I}) + \alpha w \mathcal{L}_{\text{semantic}}(\theta_e; \mathbf{I}) \right]. \quad (9)$$

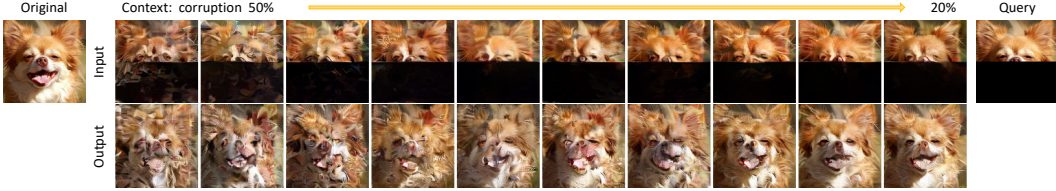


Figure 2. **An example of the conditional image denoising task** for high resolution synthesis. The context comprises images randomly corrupted in the token space.

### 3.2 Progressive In-Context Decoding

While our method is more effective when backpropagating through LLMs by prompt [23] or adapter tuning [17, 18], this work focuses on verifying the plausibility in an extreme setting of in-context learning [4]. We demonstrate that LLMs are capable of performing new tasks in foreign modalities without any parameter updates. Specifically, a set of  $K$  examples  $\{(\mathbf{u}^i, \mathbf{v}^i)\}_{i=1}^K$  are fed to the LLM to learn a new task and answer a query  $\hat{\mathbf{u}}$  with

$$\hat{\mathbf{v}} \sim \mathbb{P}_{\text{LLM}}(\cdot \mid \hat{\mathbf{u}}; \{(\mathbf{u}^i, \mathbf{v}^i)\}_{i=1}^K). \quad (10)$$

Sampling  $\hat{\mathbf{v}}$  by a single-pass autoregressive decoding is suboptimal due to the distributional shift in the representation and the presence of exceptionally long sequences, *e.g.*, an image is quantized into over 500 tokens. To this end, we use a progressive decoding method.

We generalize Eq. (10) into a multi-pass process, where the LLM learns to generate one segment of the target sequence at a time. The segment generated from the  $t$ -th pass is

$$\hat{\mathbf{v}}_t \sim \mathbb{P}_{\text{LLM}}(\cdot \mid [\hat{\mathbf{u}}, \hat{\mathbf{v}}_{<t'}]; \{([\mathbf{u}^i, \mathbf{v}_{<t'}^i], \mathbf{v}_t^i)\}_{i=1}^K), \quad (11)$$

where  $[\cdot, \cdot]$  indicates concatenation.  $t'$  controls the length of previous segments to condition on, with two common cases: (1) a progressive autoregressive (PAR) process with  $t' = t$ , where each decoded segment conditions on all previously decoded ones; (2) a progressive non-autoregressive (PNAR) process with  $t' = 0$  to sample each segment independently, which greatly reduces the sequence length requirement for the LLM. In practice, we use PAR to generate the first few token layers given task-specific conditions, followed by PNAR to generate the remaining token layers conditioned on the previous layers in an unconditional latent refinement process.

The learning capacity of an in-context setup is far from sufficient for a modality that has not been seen during training. So far, there have been no successful attempts in the literature demonstrating that a frozen LLM can generate image content. For low-resolution images, LLMs can produce images directly using in-context learning, as will be demonstrated with  $32 \times 32$  MNIST images [11]. For higher resolutions, the context length restricts the number of examples. For instance, a context window of 8k tokens can only hold less than a dozen  $128 \times 128$  images. Therefore, we operate in a denoising subspace to synthesis beyond  $32 \times 32$  resolution. Fig. 2 illustrates one example, with detailed definitions in the Appendix.

## 4 Experimental Results

### 4.1 Experimental Settings

To verify the compatibility with different LLMs, we train two variants of SPAE, namely SPAE<sub>PaLM</sub> and SPAE<sub>GPT</sub>. The SPAE<sub>PaLM</sub> codebook is taken from the input embedding layer of a PaLM 2-S checkpoint with a 65k vocabulary of the most frequent sentence pieces. The PaLM 2-L API [2] is used for in-context learning with SPAE<sub>PaLM</sub>. SPAE<sub>GPT</sub> uses a byte-pair encoding vocabulary with 99k UTF-8 tokens (<https://github.com/openai/tiktoken>), where we obtain the contextual token embeddings from OpenAI text-embedding-ada-002 (<https://platform.openai.com/docs/models/embeddings>). For a fair comparison with prior works [27], we use SPAE<sub>GPT</sub> with the GPT 3.5 text-davinci-003 API (<https://platform.openai.com/docs/models/gpt-3-5>).

We configure SPAE to encode a  $128 \times 128$  image into a token pyramid of 6 layers where each layer has  $2^k \times 2^k$  tokens and  $k = [0, 1, 2, 3, 4, 4]$ . Additionally, we train a video-based SPAE model on the Kinetics-600 dataset [5], and further details can be found in the Appendix. We apply semantic guidance loss to the first five layers, with thresholds of 0.98, 0.95, 0.9, 0.85, and 0.8. The CLIP with a ViT-L/14 [13] vision backbone is used. We use 80 prompt templates from the zero-shot ImageNet

Table 1. **Few-shot classification accuracy** on the mini-ImageNet benchmarks.  $\text{SPAE}_{\text{GPT}}$  and  $\text{SPAE}_{\text{PaLM}}$  are trained using different vocabularies and embedding sources, with different prompt templates for in-context learning. They show the broad compatibility of SPAE but are not for a comparison between the LLMs. The best performance with GPT is in italics while the overall best is in bold.

Method	# Layers : # Tokens	Task Induction Inner Shots Repeats	1	✓	✓	✓	✓	✓	✓	Avg
			0	0	0	0	1	3	5	
<i>2-Way Classification</i>										
Frozen [35]	-		1.7	33.7	66	66	63	65	63.7	51.3
LQAE [27]	1: 256	GPT 3.5	1.5	35.2	68.2	69.8	68.5	68.7	65.9	53.97
$\text{SPAE}_{\text{GPT}}$ (ours)	2: 5	GPT 3.5	5.3	77.2	84.4	86.0	79.4	77.2	77.1	69.51
$\text{SPAE}_{\text{PaLM}}$ (ours)	2: 5	PaLM 2	<b>32.2</b>	84.0	88.5	88.4	<b>85.1</b>	83.6	82.4	77.74
$\text{SPAE}_{\text{PaLM}}$ (ours)	3: 21	PaLM 2	27.9	<b>84.8</b>	<b>92.5</b>	<b>92.6</b>	84.8	<b>85.2</b>	<b>85.4</b>	<b>79.03</b>
<i>5-Way Classification</i>										
Frozen [35]	-		0.9	14.5	34.7	33.8	33.8	33.3	32.8	26.26
LQAE [27]	1: 256	GPT 3.5	1.0	15.7	35.9	36.5	31.9	36.4	45.9	29.04
$\text{SPAE}_{\text{GPT}}$ (ours)	2: 5	GPT 3.5	4.3	63.0	63.4	60.6	61.9	62.1	62.1	53.91
$\text{SPAE}_{\text{PaLM}}$ (ours)	2: 5	PaLM 2	<b>23.6</b>	64.2	68.0	69.9	63.4	62.0	60.2	58.76
$\text{SPAE}_{\text{PaLM}}$ (ours)	3: 21	PaLM 2	20.2	<b>65.1</b>	<b>73.7</b>	<b>74.3</b>	<b>66.4</b>	<b>67.0</b>	<b>66.3</b>	<b>61.86</b>

classification setup to precompute the CLIP text embeddings for the vocabulary. In addition, we use the Adam [20] optimizer with loss weights  $\alpha = 1, \beta = 0.33, \lambda = 0.1, \eta = 0.1, \phi = 10^{-4}$  and a learning rate of  $10^{-4}$  following a linear warmup/cooldown and root square decay schedule. Following the prior work [27], SPAE is trained on the ImageNet ILSVRC2012 [10] dataset. We train with a batch size of 256 for 450k steps. Further details can be found in the Appendix.

## 4.2 Main Evaluation

**Few-shot image classification.** We evaluate the in-context image understanding capability with a frozen LLM on the mini-ImageNet [40] few-shot classification benchmark. A set of tokenized images and class labels are fed to the language model as context for classification of a new image. Following [35, 27], we evaluate 14 settings controlled by four factors regarding the content of each test case: (1) task induction: whether including a preamble to specify the output space; (2) number of ways: the number of categories; (3) number of inner shots: the number of unique examples for each category; (4) number of repeats: the number of times that each unique example is repeated.

We compare SPAE with the state-of-the-art methods Frozen [35] and LQAE [27]. As shown in Tab. 1,  $\text{SPAE}_{\text{GPT}}$  consistently outperforms LQAE, both using the same GPT 3.5 model and in-context format, while using only 2% of its tokens. Fig. 3 shows the performance trend when using different number of  $\text{SPAE}_{\text{PaLM}}$  layers across six settings with task induction and 0 repeats.  $\text{SPAE}_{\text{PaLM}}$  with 3 layers achieves the best performance which balances between sufficient semantics and an image sequence length that is optimal for LLM in-context learning. Overall,  $\text{SPAE}_{\text{PaLM}}$  yields +25% and +32% average accuracy improvement over the state-of-the-art on the 2-way and 5-way benchmarks in Tab. 1.

**Reconstruction quality.** We compare the image and video reconstruction quality using the tokens produced by SPAE and the VQGAN baseline used in state-of-the-art image [7, 25, 6] and video generation [45]. We use FID [16], Inception Score (IS) [33], and LPIPS [48] to compare with the image VQGAN from MaskGIT [7] on the ImageNet validation set, and FVD [36] to compare the 3D-VQGAN from MAGVIT [45] on the Kinetics-600 validation set. The results are presented in Tab. 2. While SPAE may have more lossy reconstruction compared to VQGAN when using a similar number of tokens, this is compensated by going into deeper layers. At the bottom of Tab. 2, we showcase the scalability of our model by training on the ImageNet-21k dataset with 13M images and list the comparable variant from LDM [32] as a reference.

**Token pyramid visualization.** We visualize the tokens produced by SPAE in Fig. 4, where we show the raw pyramid or histogram of tokens with top frequencies for the first four layers, with reconstructed images from layer 5 and 6. We have the following findings.

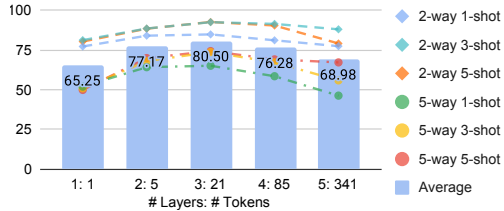


Figure 3. **Few-shot classification accuracy** on mini-ImageNet using different  $\text{SPAE}_{\text{PaLM}}$  layers.

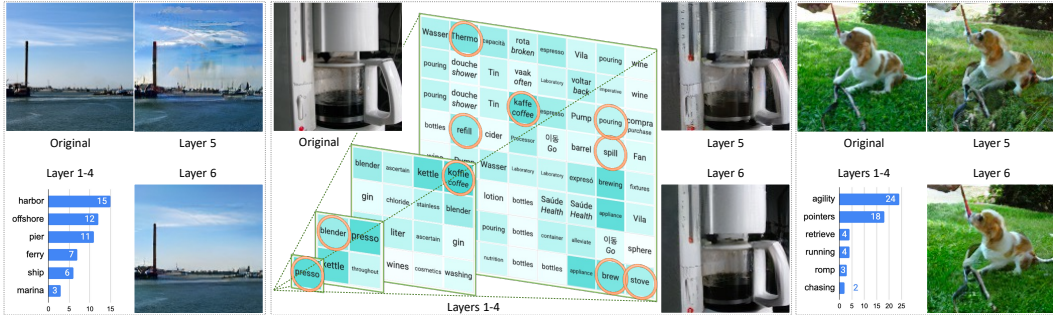


Figure 4. **Examples of pyramid image tokenization and reconstruction** by a 6-layer SPAE. We show the raw pyramid or histogram of most frequent tokens for the first four layers, and reconstructed images from layer 5 and 6. In the pyramid, we use darker cells to show tokens with higher CLIP similarity to the original image. For non-English sub-word tokens, we show automatic translation for reference in italic fonts below the original token. Circled tokens are mentioned in Section 4.2. See full pyramid visualizations in the Appendix.

Table 2. **Comparison of reconstruction quality** between SPAE and VQGAN baselines used in state-of-the-art image [7, 25, 6] and video [45] generation models.

Resolution	Method	# Layers : # Tokens	Image (ImageNet ILSVRC2012 [10])			Video (Kinetics-600 [5])
			FID↓	IS↑	LPIPS↓	FVD↓
128×128	VQGAN	1: 256	5.48	119.69	0.13	6.79
	SPAЕ (ours)	5: 341	9.49	109.46	0.17	52.28
	SPAЕ (ours)	6: 597	<b>4.41</b>	<b>133.03</b>	<b>0.12</b>	<b>6.35</b>
256×256	VQGAN	1: 256	4.04	163.95	0.21	-
	SPAЕ (ours)	6: 597	<b>3.60</b>	<b>168.50</b>	<b>0.19</b>	-
	VQGAN(LDM [32], OpenImages)	1: 256	5.15	144.53	-	-
	SPAЕ (ours, ImageNet-21k)	6: 597	3.08	173.79	0.19	-

First, the SPAE tokens are organized in a pyramid structure, with every layer comprising semantically related tokens to the image. The few tokens in the top layers seem to capture the primary theme of the image. For instance, in Fig. 4, the token *presso* (highlighted in orange) represents the espresso machine and other tokens like *blender* refer to related regions. Layer 3 and Layer 4 reveal additional details about localized objects. For example, the token *Thermo* refers to the thermometer in the top-left region, while *stove* appears in the bottom-right area. In addition to nouns, related verbs also show up, including *pouring*, *refill*, *spill*, and *brew*.

Second, it is worth noting that the CLIP model has an English-only vocabulary. However, thanks to the multilingual vocabularies and embeddings from the LLM, SPAE’s semantic guidance is able to map to similar concepts in other languages, such as *koffie* in Dutch and *kaffe* in Danish as corresponding terms to the concept of coffee.

Third, similar to RQ tokens [22], SPAE tokens can reconstruct the image with progressively refined details when more layers, and thus tokens, are utilized. Fig. 4 shows Layer 5 begins to produce a reasonable reconstruction while Layer 6 further enhances the level of detail and smoothness.

**Visual question answering.** Tab. 3 provides quantitative results on the visual question answering (VQA) task. We compare with the baseline Frozen [35] method on the Real-Fast-VQA [35] benchmark for few-shot learning. As shown, SPAE consistently outperforms Frozen. Unlike Frozen, SPAE training does not require backpropagation through the LLM.

Table 3. **Few-shot VQA performance** on Real-Fast-VQA.

Inner Shots	1	3	5
Frozen [35]	7.8	10.1	10.5
SPAЕ <sub>PaLM</sub> (ours)	<b>14.3</b>	<b>15.9</b>	<b>15.1</b>

### 4.3 Qualitative Studies

This section explores the capability of a frozen PaLM 2, trained solely on language tokens, in performing multimodal tasks using in-context learning. We adopt a two-stage decoding process for image generation. In stage one, we use AR decoding to produce the first 5 SPAE layers with task-specific conditions. Stage two is a task-agnostic NAR decoding process for layer 6 conditioned on the first 5 layers.

**Image to text and VQA.** We examine two tasks involving visual-text reasoning (1) image captioning on COCO [26] captions; and (2) visual question answering (VQA) on COCO-QA [31]. For both

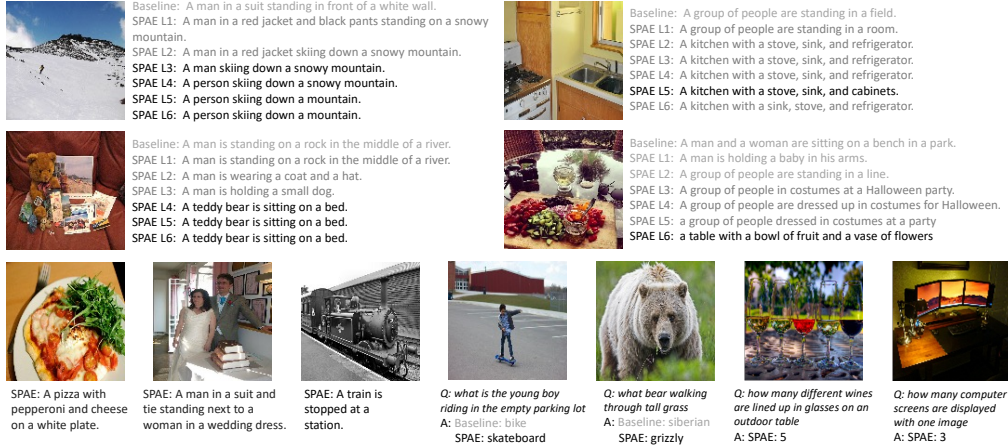


Figure 5. **Qualitative samples of image-to-text generation:** image captioning and VQA. We compare between different layers of SPAE (L1-L6) and a baseline model without semantic guidance or pyramid SAQ.

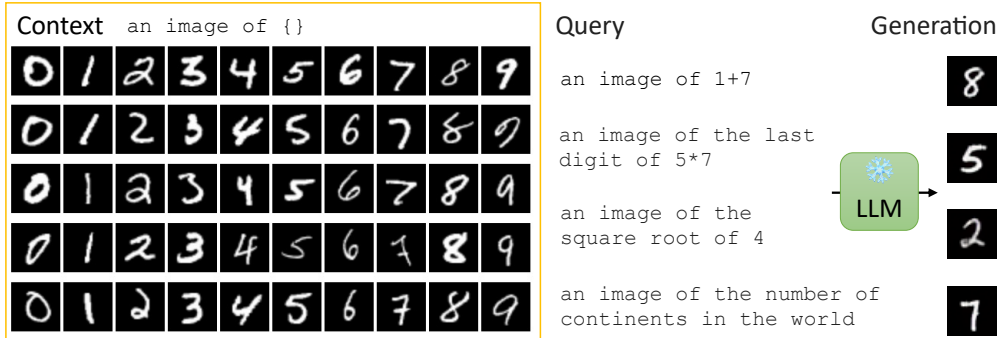


Figure 6. **Examples of text-to-image generation on MNIST** using SPAE with a frozen PaLM 2 model. We use SPAE to tokenize 50 handwritten images as the context and ask PaLM 2, an LLM trained solely on text tokens, to answer complex queries that require generating digit images through SPAE as the output.

tasks, we provide 10 unique training examples as prompts. In the case of VQA, 10 different answers are presented to form a 10-way 1-shot setup.

We compare SPAE to a baseline model trained with the same frozen language codebook but without the proposed semantic guidance or pyramid SAQ. As shown in Fig. 5, when fed with baseline tokens, the LLM randomly hallucinates a caption or guesses an answer simply based on the question. Similar hallucination can happen if we only use the first two layers of SPAE or five words to represent an image, as it provides insufficient context for captioning. Reasonable captions start to appear with 4 layers or 85 words, while complex scenes may still need the full 6 layers of 597 words.

**LLM generating MNIST images.** Fig. 6 shows a few image generation examples on MNIST [11]. The frozen LLM learns about handwritten digit images through 50 context samples tokenized by SPAE trained on MNIST. Each sample consists of a preamble "an image of  $k$ " and the lexical tokens representing an image of digit  $k$ . Then we can ask the LLM to answer questions with digit images. Specifically, with a query of "an image of 1+7", we can use progressive AR decoding with the LLM to produce a token sequence that can be decoded into an image of 8 by SPAE. We test with complex questions requiring mathematical reasoning or common sense knowledge, and the LLM is able to respond correctly. In addition, the generated digit images appear different from all context samples. This demonstrates the cross-modal reasoning capability enabled by SPAE and a frozen LLM, with images generated over the text-only interface.

**Conditional image denoising.** To the best of our knowledge, there have been no successful attempts that demonstrate generic image generation capability using a frozen LLM. To this end, we define a simpler denoising setup to explore the capability of LLMs. Fig. 7 demonstrates the conditional image denoising tasks, *e.g.*, image outpainting, deblur, inpainting, location translation, rotation, *etc.* Note that, in order to generate images for each task, we utilize 10 pairs of noisy examples with corruption rates ranging from 50% to 20%, as discussed in Section 3.2. The full context, which is omitted in Fig. 7, can be found in the Appendix.



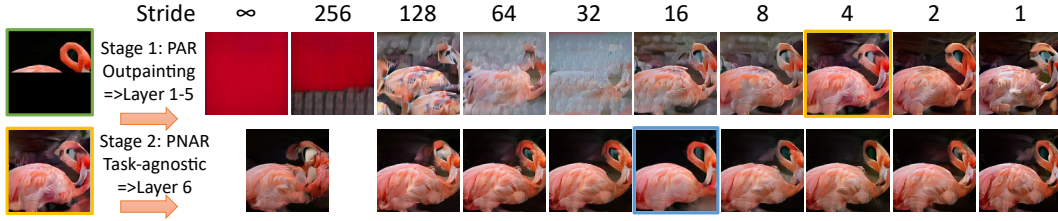


Figure 7. **Examples of conditional image denoising.** We compare different decoding strides for both stages. Yellow and blue boxes indicate the selected results. The LLM is provided with ten pairs of noisy examples like Fig. 2, which are deferred to the Appendix.

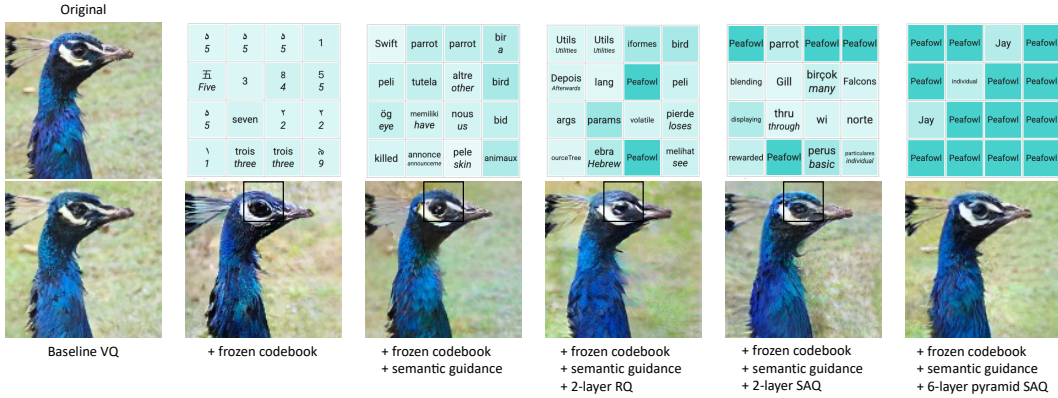


Figure 8. **Ablation examples with reconstructed image and semantic tokens** for models listed in Tab. 4. For non-pyramid tokens, we show a  $4 \times 4$  crop from the first layer corresponding to the region indicated by the black box. For pyramid tokens, we use the third layer which consists of  $4 \times 4$  tokens.

The top rows of Fig. 7 compare the generation from different decoding strides with the same set of context examples. Single-step decoding with infinity stride fails to produce a reasonable image, which validates the proposed progressive generation approach.

In Fig. 9, we qualitatively compare SPAE with baseline methods VQGAN and LQAE using the same in-context denoising procedure. As shown, VQGAN fails to produce reasonable images, in part because many words in the LLM output are out of its vocabulary. LQAE only produces vague object contours but cannot recover any visual details. On the contrary, SPAE can generate reasonable images.

**Conditional video denoising and other tasks.** Due to space constraints, we show the examples in the Appendix.

#### 4.4 Ablation Studies

The results in Tab. 4 and Fig. 8 verify the effectiveness of the proposed designs in SPAE, as evaluated by reconstruction quality (FID, IS, LPIPS) and semantic relevance (CLIP score, few-shot classification accuracy). We have the following findings. First, simply using a frozen codebook negatively affects the reconstruction results, but with semantic guidance it performs comparably with the original VQGAN while producing meaningful lexical words. Second, RQ hurts reconstruction quality with a frozen codebook. This is different from RQ’s standard setup [22] where the codebook is learned. Third, SAQ improves both quality and semantic similarity, where the pyramid enables representation with much fewer tokens. This allows for accommodating more examples within the fixed and constrained in-context length. Finally, per-layer semantic thresholds benefit understanding and the dynamic semantic loss weight helps reconstruction. The perceptual loss leverages a trained network with access to classification labels, but removing it results in a surprising improvement in classification accuracy while greatly hurting the reconstruction.

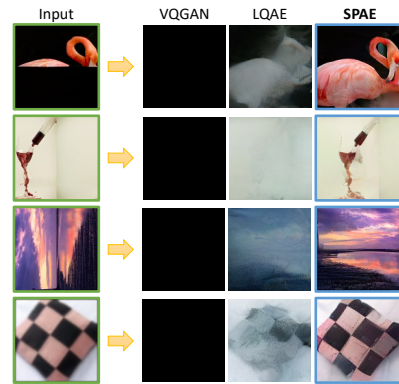


Figure 9. **Comparison on conditional image denoising with different tokenizers.** All models use the same decoding setup with the same ten pairs of prompt images available in the Appendix.

Table 4. **Ablation studies** on codebook, training objective, quantization method, and token structure. Classification accuracy is evaluated under the mini-ImageNet 5-way 1-shot setup.

Method	# Layers : # Tokens	FID↓	IS↑	LPIPS↓	CLIP↑	Classification Accuracy↑
Baseline VQ	1: 256	5.48	119.69	0.13	n/a	19.6
+ frozen codebook	1: 256	7.44	101.39	0.17	0.1464	19.5
+ semantic loss	1: 256	5.17	124.41	0.13	0.1518	46.2
+ 2-layer RQ [22]	1: 256	11.94	89.01	0.22	0.1595	56.2
	2: 512	6.05	113.93	0.15	0.1547	-
+ 2-layer SAQ	1: 256	12.30	93.33	0.21	0.1613	56.6
	2: 512	5.08	125.27	0.14	0.1595	-
	1: 1	-	-	-	<b>0.1879</b>	52.0
	2: 5	-	-	-	0.1868	64.2
+ 6-layer pyramid SAQ ( <i>SPA</i> E)	3: 21	-	-	-	0.1815	<b>65.1</b>
	4: 85	-	-	-	0.1711	58.5
	5: 341	9.49	109.46	0.17	0.1604	46.3
	6: 597	<b>4.41</b>	<b>133.03</b>	<b>0.12</b>	0.1577	-
no per-layer thresholds	6: 597	4.33	122.25	0.11	0.1650	59.4 (layer 3)
no dynamic semantic weight	6: 597	9.00	85.14	0.19	0.1847	65.1 (layer 3)
no perceptual loss	6: 597	40.47	33.41	0.20	0.1994	69.5 (layer 3)

## 5 Conclusion

Our work unveils the untapped potential of frozen Large Language Models (LLMs) in tackling multimodal understanding and generation tasks involving images and videos, without requiring explicit training on these modalities. This is achieved by a new method, *SPA*E, which converts between visual content and lexical tokens of variable length, imbued with rich semantic meaning. Our findings show the great potential of harnessing the vast knowledge and reasoning capabilities of LLMs in the field of computer vision, transcending the limitations of language-only tasks.

**Limitations.** More tokens are required to achieve the same level of reconstruction when using the frozen language codebook, compared to the existing VQGAN models with learned codebooks. The capability of in-context learning is significantly constrained by the acceptable sequence length. Although our results suggest the plausibility of image generation, the resolution, quality, and diversity is far from the recent text-to-image models trained on large image and text data.

**Broader impact.** Our paper showcases the untapped potential of frozen LLMs in multimodal understanding and generation tasks involving images and videos, without requiring explicit training on these modalities. As an initial research proof-of-concept, we focus on in-context learning, which has limitations in learning context and constrained capabilities. Consequently, there is still a substantial gap to the recent specialized models for text-to-image (*e.g.*, Stable Diffusion) or image-to-text that have been specifically trained using billions of text-image pairs.

The potential impact of our research lies in its influence on future studies, specifically in the area of integrating vision modalities into the LLMs. For instance, our work can be extended to explore finetuning or adapter tuning of LLMs on large-scale text-image datasets. Future research in these directions may implicate ethical issues around fairness and transparency. We have found that the generated tokens occasionally include slang terms or words that create inappropriate connotations related to the subject depicted in the image or video. Such concerns must be thoroughly considered and effectively addressed prior to deploying this method in real-world applications.

**Acknowledgments and disclosure of funding.** The authors would like to thank anonymous reviewers and area chairs their insightful comments, and to Siamak Shakeri, Sergey Ioffe, Jay Yagnik, and Boqing Gong for their valuable feedback and constructive discussions. This project is funded in part by Carnegie Mellon University’s Mobility21 National University Transportation Center, which is sponsored by the US Department of Transportation.

## References

- [1] Jean-Baptiste Alayrac, Jeff Donahue, Pauline Luc, Antoine Miech, Iain Barr, Yana Hasson, Karel Lenc, Arthur Mensch, Katherine Millican, Malcolm Reynolds, et al. Flamingo: a visual language model for few-shot learning. In *NeurIPS*, 2022. 3
- [2] Rohan Anil, Andrew M Dai, Orhan Firat, Melvin Johnson, Dmitry Lepikhin, Alexandre Passos, Siamak Shakeri, Emanuel Taropa, Paige Bailey, Zhifeng Chen, et al. PaLM 2 technical report. *arXiv:2305.10403*, 2023. 1, 2, 3, 5
- [3] Zalán Borsos, Raphaël Marinier, Damien Vincent, Eugene Kharitonov, Olivier Pietquin, Matt Sharifi, Dominik Roblek, Olivier Teboul, David Grangier, Marco Tagliasacchi, et al. AudioLM: a language modeling approach to audio generation. *IEEE/ACM Transactions on Audio, Speech, and Language Processing*, 2023. 2
- [4] Tom Brown, Benjamin Mann, Nick Ryder, Melanie Subbiah, Jared D Kaplan, Prafulla Dhariwal, Arvind Neelakantan, Pranav Shyam, Girish Sastry, Amanda Askell, et al. Language models are few-shot learners. In *NeurIPS*, 2020. 1, 2, 3, 5
- [5] Joao Carreira, Eric Noland, Andras Banki-Horvath, Chloe Hillier, and Andrew Zisserman. A short note about Kinetics-600. *arXiv:1808.01340*, 2018. 5, 7
- [6] Huiwen Chang, Han Zhang, Jarred Barber, AJ Maschinot, Jose Lezama, Lu Jiang, Ming-Hsuan Yang, Kevin Murphy, William T Freeman, Michael Rubinstein, et al. Muse: Text-to-image generation via masked generative transformers. In *ICML*, 2023. 6, 7
- [7] Huiwen Chang, Han Zhang, Lu Jiang, Ce Liu, and William T Freeman. MaskGIT: Masked generative image transformer. In *CVPR*, 2022. 2, 6, 7
- [8] Aakanksha Chowdhery, Sharan Narang, Jacob Devlin, Maarten Bosma, Gaurav Mishra, Adam Roberts, Paul Barham, Hyung Won Chung, Charles Sutton, Sebastian Gehrmann, et al. PaLM: Scaling language modeling with pathways. *arXiv:2204.02311*, 2022. 1, 3
- [9] Alexandre Défossez, Jade Copet, Gabriel Synnaeve, and Yossi Adi. High fidelity neural audio compression. *arXiv:2210.13438*, 2022. 2
- [10] Jia Deng, Wei Dong, Richard Socher, Li-Jia Li, Kai Li, and Li Fei-Fei. ImageNet: A large-scale hierarchical image database. In *CVPR*, 2009. 6, 7
- [11] Li Deng. The mnist database of handwritten digit images for machine learning research [best of the web]. *IEEE Signal Processing Magazine*, 29(6):141–142, 2012. 5, 8
- [12] Jacob Devlin, Ming-Wei Chang, Kenton Lee, and Kristina Toutanova. BERT: Pre-training of deep bidirectional transformers for language understanding. In *NAACL*, 2019. 3
- [13] Alexey Dosovitskiy, Lucas Beyer, Alexander Kolesnikov, Dirk Weissenborn, Xiaohua Zhai, Thomas Unterthiner, Mostafa Dehghani, Matthias Minderer, Georg Heigold, Sylvain Gelly, et al. An image is worth 16x16 words: Transformers for image recognition at scale. In *ICLR*, 2020. 5
- [14] Patrick Esser, Robin Rombach, and Bjorn Ommer. Taming transformers for high-resolution image synthesis. In *CVPR*, 2021. 2
- [15] Songwei Ge, Thomas Hayes, Harry Yang, Xi Yin, Guan Pang, David Jacobs, Jia-Bin Huang, and Devi Parikh. Long video generation with time-agnostic VQGAN and time-sensitive transformer. In *ECCV*, 2022. 2, 4
- [16] Martin Heusel, Hubert Ramsauer, Thomas Unterthiner, Bernhard Nessler, and Sepp Hochreiter. Gans trained by a two time-scale update rule converge to a local nash equilibrium. In *NeurIPS*, 2017. 6
- [17] Neil Houlsby, Andrei Giurgiu, Stanislaw Jastrzebski, Bruna Morrone, Quentin De Laroussilhe, Andrea Gesmundo, Mona Attariyan, and Sylvain Gelly. Parameter-efficient transfer learning for nlp. In *ICLR*, 2019. 5
- [18] Edward J Hu, Yelong Shen, Phillip Wallis, Zeyuan Allen-Zhu, Yuanzhi Li, Shean Wang, Lu Wang, and Weizhu Chen. Lora: Low-rank adaptation of large language models. In *ICLR*, 2021. 5
- [19] Justin Johnson, Alexandre Alahi, and Li Fei-Fei. Perceptual losses for real-time style transfer and super-resolution. In *ECCV*, 2016. 4
- [20] Diederik P Kingma and Jimmy Ba. Adam: A method for stochastic optimization. *arXiv:1412.6980*, 2014. 6
- [21] Jing Yu Koh, Ruslan Salakhutdinov, and Daniel Fried. Grounding language models to images for multi-modal generation. In *ICML*, 2023. 1, 2, 3
- [22] Doyup Lee, Chiheon Kim, Saehoon Kim, Minsu Cho, and Wook-Shin Han. Autoregressive image generation using residual quantization. In *CVPR*, 2022. 3, 4, 7, 9, 10

- [23] Brian Lester, Rami Al-Rfou, and Noah Constant. The power of scale for parameter-efficient prompt tuning. In *EMNLP*, 2021. 5
- [24] Aitor Lewkowycz, Anders Andreassen, David Dohan, Ethan Dyer, Henryk Michalewski, Vinay Ramasesh, Ambrose Slone, Cem Anil, Imanol Schlag, Theo Gutman-Solo, et al. Solving quantitative reasoning problems with language models. In *NeurIPS*, 2022. 3
- [25] Jose Lezama, Tim Salimans, Lu Jiang, Huiwen Chang, Jonathan Ho, and Irfan Essa. Discrete predictor-corrector diffusion models for image synthesis. In *ICLR*, 2023. 6, 7
- [26] Tsung-Yi Lin, Michael Maire, Serge Belongie, James Hays, Pietro Perona, Deva Ramanan, Piotr Dollár, and C Lawrence Zitnick. Microsoft coco: Common objects in context. In *ECCV*, 2014. 7
- [27] Hao Liu, Wilson Yan, and Pieter Abbeel. Language quantized autoencoders: Towards unsupervised text-image alignment. *arXiv:2302.00902*, 2023. 1, 2, 3, 5, 6
- [28] OpenAI. GPT-4 technical report. *arXiv:2303.08774*, 2023. 1, 2
- [29] Alec Radford, Jong Wook Kim, Chris Hallacy, Aditya Ramesh, Gabriel Goh, Sandhini Agarwal, Girish Sastry, Amanda Askell, Pamela Mishkin, Jack Clark, et al. Learning transferable visual models from natural language supervision. In *ICML*, 2021. 4
- [30] Aditya Ramesh, Mikhail Pavlov, Gabriel Goh, Scott Gray, Chelsea Voss, Alec Radford, Mark Chen, and Ilya Sutskever. Zero-shot text-to-image generation. In *ICML*, 2021. 2
- [31] Mengye Ren, Ryan Kiros, and Richard Zemel. Exploring models and data for image question answering. In *NeurIPS*, 2015. 7
- [32] Robin Rombach, Andreas Blattmann, Dominik Lorenz, Patrick Esser, and Björn Ommer. High-resolution image synthesis with latent diffusion models. In *CVPR*, 2022. 2, 6, 7
- [33] Tim Salimans, Ian Goodfellow, Wojciech Zaremba, Vicki Cheung, Alec Radford, and Xi Chen. Improved techniques for training gans. In *NeurIPS*, 2016. 6
- [34] Hung-Yu Tseng, Lu Jiang, Ce Liu, Ming-Hsuan Yang, and Weilong Yang. Regularizing generative adversarial networks under limited data. In *CVPR*, 2021. 4
- [35] Maria Tsimpoukelli, Jacob L Menick, Serkan Cabi, SM Eslami, Oriol Vinyals, and Felix Hill. Multimodal few-shot learning with frozen language models. In *NeurIPS*, 2021. 6, 7
- [36] Thomas Unterthiner, Sjoerd van Steenkiste, Karol Kurach, Raphael Marinier, Marcin Michalski, and Sylvain Gelly. Towards accurate generative models of video: A new metric & challenges. *arXiv:1812.01717*, 2018. 6
- [37] Aaron Van Den Oord, Oriol Vinyals, et al. Neural discrete representation learning. In *NeurIPS*, 2017. 2, 3
- [38] Ashish Vaswani, Noam Shazeer, Niki Parmar, Jakob Uszkoreit, Llion Jones, Aidan N Gomez, Łukasz Kaiser, and Illia Polosukhin. Attention is all you need. In *NeurIPS*, 2017. 1
- [39] Ruben Villegas, Mohammad Babaeizadeh, Pieter-Jan Kindermans, Hernan Moraldo, Han Zhang, Mohammad Taghi Saffar, Santiago Castro, Julius Kunze, and Dumitru Erhan. Phenaki: Variable length video generation from open domain textual description. *arXiv:2210.02399*, 2022. 2
- [40] Oriol Vinyals, Charles Blundell, Timothy Lillicrap, Daan Wierstra, et al. Matching networks for one shot learning. In *NeurIPS*, 2016. 6
- [41] Alex Wang, Yada Pruksachatkun, Nikita Nangia, Amanpreet Singh, Julian Michael, Felix Hill, Omer Levy, and Samuel Bowman. SuperGLUE: A stickier benchmark for general-purpose language understanding systems. In *NeurIPS*, 2019. 3
- [42] Jason Wei, Yi Tay, Rishi Bommasani, Colin Raffel, Barret Zoph, Sebastian Borgeaud, Dani Yogatama, Maarten Bosma, Denny Zhou, Donald Metzler, et al. Emergent abilities of large language models. *TMLR*, 2022. 1
- [43] Chenfei Wu, Shengming Yin, Weizhen Qi, Xiaodong Wang, Zecheng Tang, and Nan Duan. Visual ChatGPT: Talking, drawing and editing with visual foundation models. *arXiv:2303.04671*, 2023. 2
- [44] Pengcheng Yin, Wen-Ding Li, Kefan Xiao, Abhishek Rao, Yeming Wen, Kensen Shi, Joshua Howland, Paige Bailey, Michele Catasta, Henryk Michalewski, et al. Natural language to code generation in interactive data science notebooks. *arXiv:2212.09248*, 2022. 3
- [45] Lijun Yu, Yong Cheng, Kihyuk Sohn, José Lezama, Han Zhang, Huiwen Chang, Alexander G Hauptmann, Ming-Hsuan Yang, Yuan Hao, Irfan Essa, et al. MAGVIT: Masked generative video transformer. In *CVPR*, 2023. 2, 4, 6, 7
- [46] Lijun Yu, José Lezama, Nitesh B Gundavarapu, Luca Versari, Kihyuk Sohn, David Minnen, Yong Cheng, Agrim Gupta, Xiuye Gu, Alexander G Hauptmann, et al. Language model beats diffusion+tokenizer is key to visual generation. *arXiv:2310.05737*, 2023. 2

- [47] Neil Zeghidour, Alejandro Luebs, Ahmed Omran, Jan Skoglund, and Marco Tagliasacchi. Soundstream: An end-to-end neural audio codec. *IEEE/ACM Trans. on Audio, Speech, and Language Processing*, 30:495–507, 2021. [3](#), [4](#)
- [48] Richard Zhang, Phillip Isola, Alexei A Efros, Eli Shechtman, and Oliver Wang. The unreasonable effectiveness of deep features as a perceptual metric. In *CVPR*, 2018. [6](#)
- [49] Susan Zhang, Stephen Roller, Naman Goyal, Mikel Artetxe, Moya Chen, Shuohui Chen, Christopher Dewan, Mona Diab, Xian Li, Xi Victoria Lin, et al. OPT: Open pre-trained transformer language models. *arXiv:2205.01068*, 2022. [2](#)

# SPAE: Semantic Pyramid AutoEncoder for Multimodal Generation with Frozen LLMs Supplementary Materials

## Appendix Overview

This supplementary document provides additional details to support our main manuscript, organized as follows:

- Appendix A presents more details on the method, including SPAE architecture designs.
- Appendix B provides additional implementation details, including a video SPAE variant.
- Appendix C includes more quantitative evaluation results.
- Appendix D shows more qualitative examples of model generations.

## A Method Details

We present additional details about the SPAE model in this section.

**Token pyramid.** Fig. 10 shows an example of the dilation subsampler defined by Eq. (1). We select evenly distributed positions in each layer to form the token pyramid with monotonically increasing layer sizes.

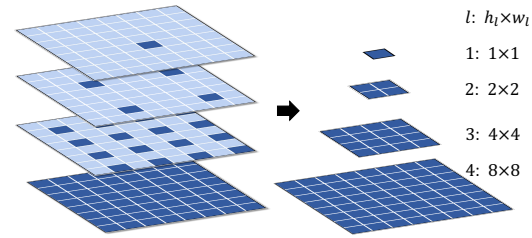


Figure 10. Dilation subsampler visualization.

**Streaming average quantization.** Fig. 11 compares our proposed Streaming Average Quantization (SAQ) with Residual Quantization (RQ) [7, 11]. At layer 2, the SAQ remainder embedding  $z_2 = 2z - e(k_1)$  is at a more similar scale to  $z$ , compared to the RQ remainder  $z - e(k_1)$ . We find that the scale consistency promotes better utilization of the frozen language codebook despite a large number of layers being used. Due to the pyramid structure, quantization in the first few layers may be skipped for those positions not selected by the dilation subsampler. Considering the scale consistency across quantization layers, the use of SAQ is more appropriate in this case.

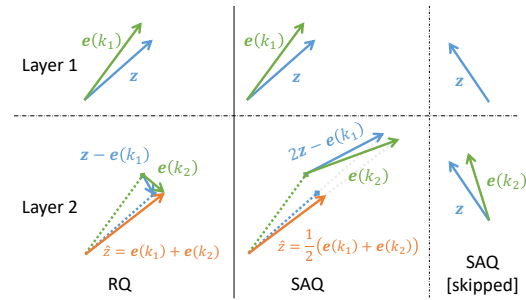


Figure 11. **Comparison between RQ and SAQ.** We show a 2-layer quantization process in a 2-dimensional space as an example. At layer  $l$ , we use blue for the current remainder embeddings  $z_l$ , green for current post-quantization embeddings  $e(k_l)$ , and orange for the reconstructed embeddings up to layer  $l$  as  $\hat{z}_{\leq l}$ .

**In-context denoising.** Take the image-to-image task in Fig. 2 as an example. The provided context are images randomly corrupted in the token space by  $\epsilon(\cdot; r)$ , where the corruption ratio  $r$  follows a cosine schedule [2].

$$(\mathbf{u}^i, \mathbf{v}^i) \sim \left( \epsilon(\mathcal{T}(\text{mask}(\mathbf{I})); r_i), \epsilon(\mathcal{T}(\mathbf{I}); r_i) \right), \mathbf{I} \in \mathcal{M} \quad (12)$$

where  $\mathcal{T}(\cdot)$  represents the SPAE tokenizer and  $\mathcal{M}$  is a small set of raw images.  $\text{mask}(\cdot)$  zeros out pixels of the real image to create the condition image, such as masking out the bottom half for

out-painting. The query  $\hat{u}$  is always sampled from  $\mathcal{M}$  without noise  $\epsilon$ . To ensure the generation is not simply copying the context, we enforce a minimal corruption rate of 20% such that no identical image from the context matches the real target image.

## B Implementation Details

### B.1 SPAE Training

**Image SPAE.** An image SPAE encodes a  $128 \times 128$  image into  $16 \times 16$  embeddings. Following the VQGAN [5] architecture, we use 128 base filters with channel multipliers [1, 2, 2, 4] and 2 residual blocks at each scale, which results in 59M parameters in total.

**Image SPAE-8.** In addition to the primary SPAE model with six pyramid layers studied in the main paper, we also train an SPAE-8 model with eight layers to conduct a more in-depth analysis of the coarse-to-fine reconstruction process. The two extra layers each contain  $16 \times 16$  tokens. The semantic loss is still applied on the first 5 layers as in the primary model.

**MNIST SPAE.** We train another SPAE on the MNIST [4] dataset with the same architecture setup. We pad the handwritten digit images from  $28 \times 28$  to  $32 \times 32$  pixels, which are then encoded into  $4 \times 4$  embeddings. Each image is represented by 37 tokens organized in four layers, with sizes of  $1 \times 1$ ,  $2 \times 2$ ,  $4 \times 4$ , and  $4 \times 4$ . We replace the CLIP image embedding with the CLIP text embedding of the label for the semantic loss. The model is trained for 10k steps with a batch size of 256. For in-context generation, AR decoding with a stride of 4 is used to produce all 37 tokens.

**Video SPAE.** We initialize a video SPAE by VQGAN inflation [10] from a pretrained image SPAE, which encodes 16 frames at  $128 \times 128$  resolution into  $4 \times 16 \times 16$  embeddings. A video SPAE consists of 176M parameters. The pyramid layers contain  $1 \times 1 \times 1$ ,  $1 \times 2 \times 2$ ,  $1 \times 4 \times 4$ ,  $2 \times 8 \times 8$ ,  $4 \times 16 \times 16$ , and  $4 \times 16 \times 16$  tokens. The video embedding is obtained as the average CLIP embedding for all frames. The model is trained on the Kinetics-600 [1] dataset which contains 384k videos. We train with a batch size of 512 for 130k steps, which takes 5.8k TPUv4-hours.

### B.2 LLM Prompting

To generate prompts, we utilize SPAE to quantize an image, or another non-linguistic modality, into a pyramid of lexical tokens. Subsequently, we flatten the tokens by concatenating them layer-by-layer, following a raster scan, and resulting in a 1-D string. This string, representing the image, is referred to as the *SPAE string* in the following prompts.

We use task-specific prompt templates to facilitate answer generation with LLMs. The LLM output is always parsed by removing leading and trailing whitespace or newline characters.

**Image classification with GPT 3.5.** We use the same prompt template as LQAE [8] to interact with GPT 3.5. For a 2-way 1-shot classification between class *lion* and *vase*, the prompt is

```
For each of the following input output pairs, output is one of ['lion', 'vase']  
###  
Input: <SPAE string from a lion image>  
Output: lion  
###  
Input: <SPAE string from a vase image>  
Output: vase  
###  
Input: <SPAE string from the query image>  
Output:
```

We use greedy decoding to get a maximum of 7 tokens from GPT 3.5.

**Image classification with PaLM 2.** We use the original miniImageNet [9] format with PaLM 2. The prompt looks like

Answer with "lion" or "vase".

<SPAE string from a lion image>  
This is a lion

<SPAE string from a vase image>  
This is a vase

<SPAE string from the query image>  
What is this? # Only used in 5-way 3/5-shot setups  
This is a

We use greedy decoding to get a maximum of 4 tokens from PaLM 2.

**Image captioning.** We use greedy decoding to get a maximum of 20 tokens before the first newline character with the following prompt:

Generate a caption sentence based on words describing an image.

Q: <SPAE string from image 1>  
A: <Caption for image 1>

Q: <SPAE string from image 2>  
A: <Caption for image 2>

Q: <SPAE string from the query image>  
A:

**Visual question answering.** We use greedy decoding to get a maximum of 4 tokens before the first newline character with the prompt template as

Answer with a single word.

C: <SPAE string from image 1>  
Q: <Question for image 1>  
A: <Answer for image 1>

C: <SPAE string from image 2>  
Q: <Question for image 2>  
A: <Answer for image 2>

C: <SPAE string from the query image>  
Q: <Question for the query image>  
A:

**Image/video generation with PAR decoding.** For image or video generation tasks, the condition can be a text string or an SPAE string of a condition image. Suppose we use PAR decoding with a stride of 4 tokens. At the 4th step, the prompt looks like

Learn a new language and predict the 4 tokens following the examples.

C:<condition for image 1>  
Q:<SPAE string (token 1-12) for image 1>  
A:<SPAE string (token 13-16) for image 1>

C:<condition for image 2>  
Q:<SPAE string (token 1-12) for image 2>  
A:<SPAE string (token 13-16) for image 2>



C:<condition for the query>  
 Q:<SPAE string (token 1-12) for the generated image from previous steps>  
 A:

We use PaLM 2 to generate 8 predicted sequences for the next 4 tokens, starting with a temperature  $T_0 = 0$ . We use the sentence piece [6] tokenizer to tokenize the output string. If all predictions are shorter than 4 tokens, we retry the LLM prediction with a higher temperature. At the  $i$ -th retry, the temperature is given by

$$T_i = \psi \sum_{j=1}^i 2^j \quad (13)$$

where  $\psi = 0.01$  is used.

**Image/video generation with PNAR decoding.** We use PNAR decoding to generate SPAE layer 6 conditioned on layer 1-5. With a stride of 16, the prompt at the 3rd step looks like

Predict the outputs following the examples.

Q:<SPAE string from layer 1-5 for image 1>  
 A:<SPAE string from layer 6 (token 33-48) for image 1>

Q:<SPAE string from layer 1-5 for image 2>  
 A:<SPAE string from layer 6 (token 33-48) for image 2>

Q:<SPAE string from layer 1-5 for the generated image from AR decoding>  
 A:

We use PaLM 2 to generate 8 predicted sequences for the next 16 tokens. If the sentence piece parsing fails, we retry with the same temperature schedule as in PAR decoding.

### B.3 Corruption Functions

**Pixel-space transformation.** We use pixel-space transformation in the conditional image interpolation tasks with the following setups:

- Brightness:  $[\pm 0.8, \pm 0.6, \pm 0.4, \pm 0.2]$ .
- Contrast:  $[\pm 0.8, \pm 0.6, \pm 0.4, \pm 0.2]$ .
- Saturation:  $[\pm 0.4, \pm 0.3, \pm 0.2, \pm 0.1]$ .
- Color (RGB):  $[(0.6, 1.4, 1), (0.7, 1.3, 1), (0.8, 1.2, 1), (0.9, 1.1, 1), (1.1, 0.9, 1), (1.2, 0.8, 1), (1.3, 0.7, 1), (1.4, 0.6, 1)]$

Overflow pixels are clipped to  $[0, 255]$ .

**Token-space permutation noise.** Random permutation is used in the in-context denoising setup for conditional image denoising tasks. Specifically, we replace a fraction of tokens each with a random token sampled from the entire 65k vocabulary to satisfy a given corruption rate. The corruption rates for the 10 examples are  $[0.5, 0.47, 0.44, 0.41, 0.38, 0.35, 0.32, 0.29, 0.26, 0.23]$ . The permutation noise presents a context distribution with expectation at the real image, but does not contain the ground truth tokens to prevent information leakage.

## C Additional Quantitative Results

**Few-shot image classification with different SPAE layers.** Tab. 5 present the few-shot mini-ImageNet classification performance with each SPAE<sub>PaLM</sub> layer. These detailed quantitative numbers accompany the findings from Fig. 3. As shown, Layer 3 achieves the best overall performance as well as in most of the setups, which balances between the level of details and the burden of the LLM.

Table 5. **Few-shot classification accuracy** on the mini-ImageNet benchmarks. - means value unavailable due to an infeasible sequence length.

Method	# Layers : # Tokens	Task Induction Inner Shots Repeats	1	✓	✓	✓	✓	✓	✓	Avg
			0	1	3	5	1	1	1	
<i>2-Way Classification</i>										
$SPAE_{PaLM}$	1: 1	PaLM 2	<b>34.8</b>	77.2	81.2	80.3	74.0	73.2	71.5	70.31
$SPAE_{PaLM}$	2: 5	PaLM 2	32.2	84.0	88.5	88.4	<b>85.1</b>	83.6	82.4	77.74
$SPAE_{PaLM}$	3: 21	PaLM 2	27.9	<b>84.8</b>	<b>92.5</b>	<b>92.6</b>	84.8	<b>85.2</b>	<b>85.4</b>	<b>79.03</b>
$SPAE_{PaLM}$	4: 85	PaLM 2	22.8	81.1	91.4	90.4	82.6	84.3	84.7	76.76
$SPAE_{PaLM}$	5: 341	PaLM 2	21.2	77.4	88.0	79.1	84.8	74.0	76.1	71.51
$SPAE_{PaLM}$	6: 597	PaLM 2	21.8	73.8	70.8	62.4	64.8	62.1	58.6	59.19
$SPAE_{PaLM}^{disjoint}$	2: 5	PaLM 2	24.8	79.8	84.5	83.7	80.8	78.5	78.4	72.93
$SPAE_{PaLM}^{disjoint}$	3: 21	PaLM 2	21.4	81.4	89.2	87.9	82.6	81.7	80.6	74.98
<i>5-Way Classification</i>										
$SPAE_{PaLM}$	1: 1	PaLM 2	<b>26.8</b>	52.0	50.9	49.9	51.9	48.4	47.9	46.83
$SPAE_{PaLM}$	2: 5	PaLM 2	23.6	64.2	68.0	69.9	63.4	62.0	60.2	58.76
$SPAE_{PaLM}$	3: 21	PaLM 2	20.2	<b>65.1</b>	<b>73.7</b>	<b>74.3</b>	<b>66.4</b>	<b>67.0</b>	66.3	<b>61.86</b>
$SPAE_{PaLM}$	4: 85	PaLM 2	16.1	58.5	67.2	69.1	64.0	66.4	<b>67.4</b>	58.39
$SPAE_{PaLM}$	5: 341	PaLM 2	12.1	46.3	55.9	67.2	43.3	46.3	-	-
$SPAE_{PaLM}$	6: 597	PaLM 2	12.1	35.7	-	-	-	-	-	-

Table 6. **Reconstruction quality and semantic relevance** of SPAE-8 tokens.

Model	# Layers : # Tokens	FID↓	IS↑	LPIPS↓	CLIP↑	Relative CLIP↑
SPAE-8	1: 1	-	-	-	<b>0.2051</b>	<b>0.8018</b>
	2: 5	-	-	-	0.2046	0.7994
	3: 21	-	-	-	0.2012	0.7834
	4: 85	-	-	-	0.1896	0.7289
	5: 341	43.42	49.78	0.32	0.1709	0.6412
	6: 597	8.93	116.12	0.18	0.1667	0.6213
	7: 853	4.78	135.01	0.13	0.1647	0.6119
	8: 1109	<b>3.89</b>	<b>140.55</b>	<b>0.11</b>	0.1634	0.6058

**Few-shot image classification with  $SPAE^{disjoint}$ .** Following the previous work of LQAE [8], we train our SPAE on the ImageNet training split [3] and present the comparative results in the main paper. There is a possibility of overlap between the training split of ImageNet and the mini-ImageNet dataset used in the few-shot classification task [9]. Since few studies have investigated this before, we present the results of training SPAE on the ImageNet training split after excluding the 20 classes used in the few-shot mini-ImageNet classification task. This creates a even more challenging setting as the visual classes have never been seen during the training of the tokenizer or the LLMs.

As demonstrated in Tab. 5, we present the results of training our tokenizer on the *disjointed* data, referred to as  $SPAE^{disjoint}$ . As expected, we observe a slight decrease in performance, since both SPAE and LLMs need to generalize to the test classes that are outside the training data distribution. Despite the fact that the baseline is trained on unlabeled images sampled from the mini-ImageNet test classes,  $SPAE_{PaLM}^{disjoint}$  still demonstrates a significant improvement over the state-of-the-art baseline on the 2-way benchmarks.

**Token quality with more SPAE layers.** Tab. 6 shows the per-layer reconstruction quality and semantic relevance of tokens from the SPAE-8 model in comparison to the default model. With more token layers, the model gains larger capacity for both semantic and appearance, where the appearance gets pushed into deeper layers. At layer 1 to 6, SPAE-8 yields consistently higher CLIP scores than SPAE. At the last three layers, SPAE-8 also has better reconstruction quality than the last two layers

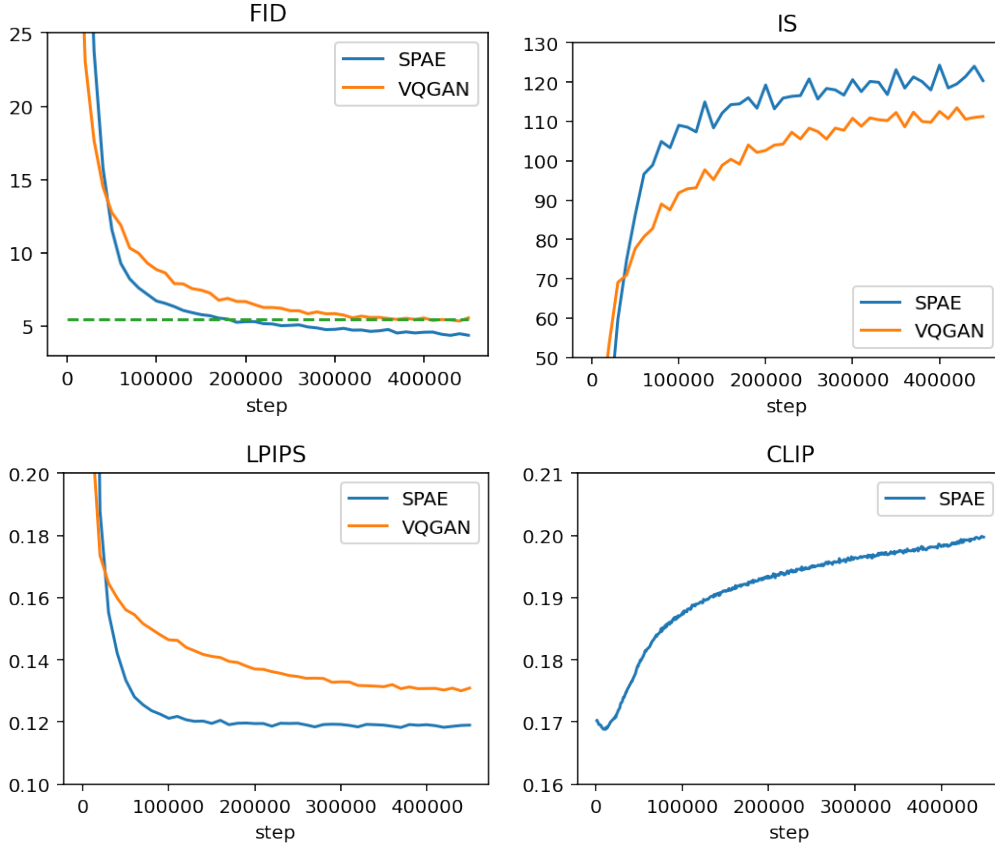


Figure 12. **Training curves** of SPAE in comparison to VQGAN. Metrics are presented regarding reconstruction quality (FID, IS, LPIPS) and semantic relevance (CLIP).

of SPAE. These results suggest the potential of better reconstruction quality and semantic relevance from using more token layers.

**Training efficiency.** All models used in the ablation study in Tab. 3, including VQGAN [5] and RQ-VAE [7] variants, are trained using the same setup for fair comparisons. Fig. 12 compares the training curves of FID, IS, LPIPS, and CLIP score of SPAE and VQGAN. As shown, within 40% of the training steps, SPAE shows better FID than the final VQGAN checkpoint. The CLIP score keeps improving as the training proceeds, while the LPIPS saturates quite early.

## D Additional Qualitative Examples

**Token pyramid visualization.** Fig. 13 shows tokenization and reconstruction samples by a 6-layer SPAE from ImageNet validation set. Key concepts are captured in the first few layers, whereas the later layers focus on the visual appearance. In the coffee machine example, many keywords are present to describe various aspects from the stove to the thermometer. In the parrot case, a single unified concept is repeatedly highlighted.

**Coarse-to-fine reconstruction.** Fig. 14 shows reconstruction samples by SPAE-8 from ImageNet validation set. We compare the reconstructed images from layer 5 to layer 8 to demonstrate the coarse-to-fine progress.

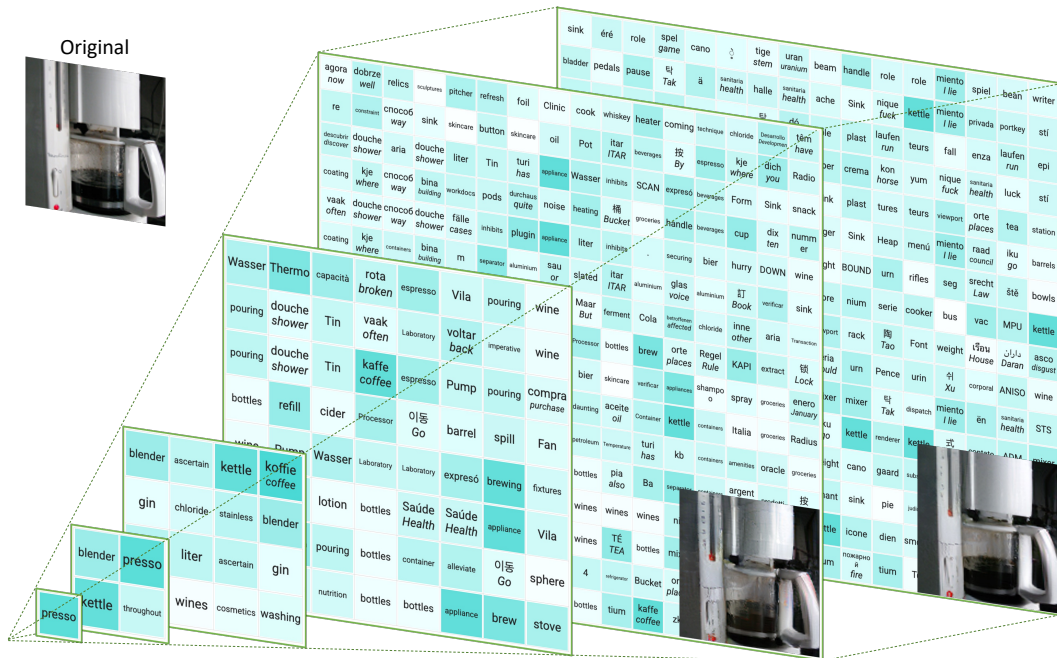
**Conditional image interpolation.** To the best of our knowledge, there have been no successful attempts that demonstrate generic image generation capability using a frozen LLM. To this end, we define a very simple setup to explore the interpolation capability of LLM, where the conditions are

integers from 1 to 9. The target images are created with different pixel-space transformations detailed in . As shown in Fig. 15, images 1-4 and 6-9 are fed as context to produce image 5, where the model interpolates the variable property. Fig. 16 shows generated samples at  $256 \times 256$  resolution under the same setup.

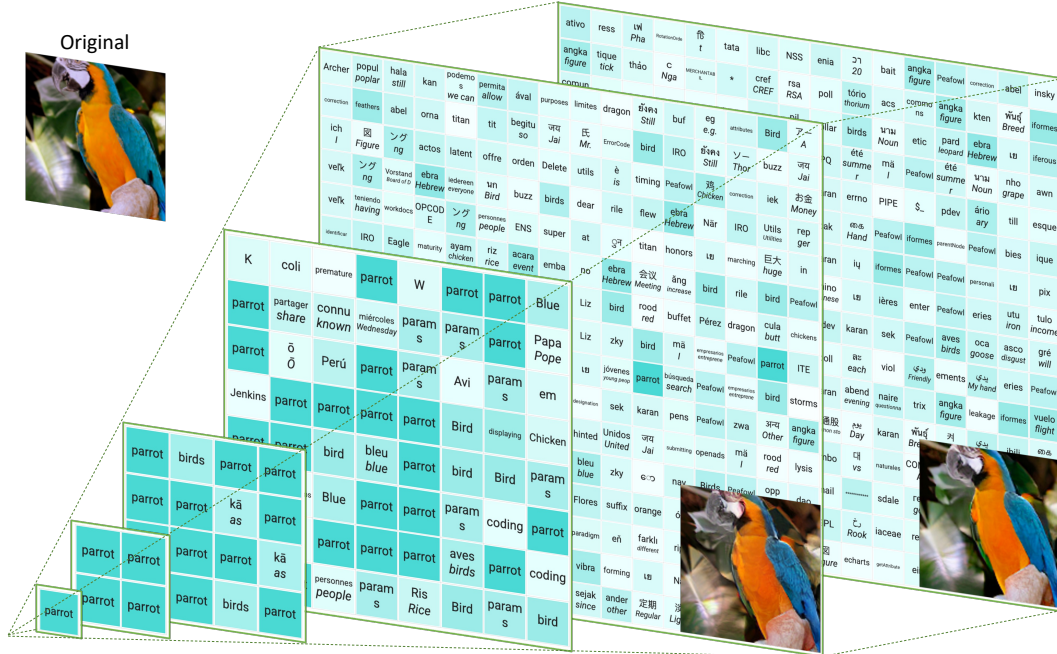
**Conditional image denoising.** We use PAR decoding to produce the first 5 token layers with task-specific conditions, followed by task-agnostic PNAR decoding to fill in layer 6. Fig. 17 visualizes the input pairs for the image-to-image generation examples in Figs. 7 and 9, with more examples in Fig. 18. Under the in-context denoising setup, the LLM generates novel images based on the provided context, where multiple different generations can be obtained.

**Multimodal outputs.** Fig. 19 shows a task requiring a single LLM to output both image and text, where it first inpaints the center region of an image using in-context denoising and then creates multiple captions for the output image.

**Image-to-video denoising.** Fig. 20 shows an image-to-video example with the frame prediction task using progressive in-context denoising. The input is one frame tokenized by the image SPAE, while the output is a 16-frame clip tokenized by the video SPAE. We follow the same two-stage procedure as image-to-image generation, with more steps in each stage to account for the longer sequence. Due to the sequence length limit, only four samples can be fit into the context, which limits LLM’s performance for this task.



(a) Many keywords are present to describe various aspects from the stove to the thermometer.



(b) A single unified concept is repeatedly highlighted.

Figure 13. **Examples of multi-layer image tokenization and reconstruction** by a 6-layer SPAE. For visualization purposes only, we use darker cells to show tokens with higher CLIP scores regarding the original image. For non-English sub-word tokens, we show automatic translation for reference in italic fonts below the original token. We show tokens in all six layers, along with reconstructed images from the last two layers.

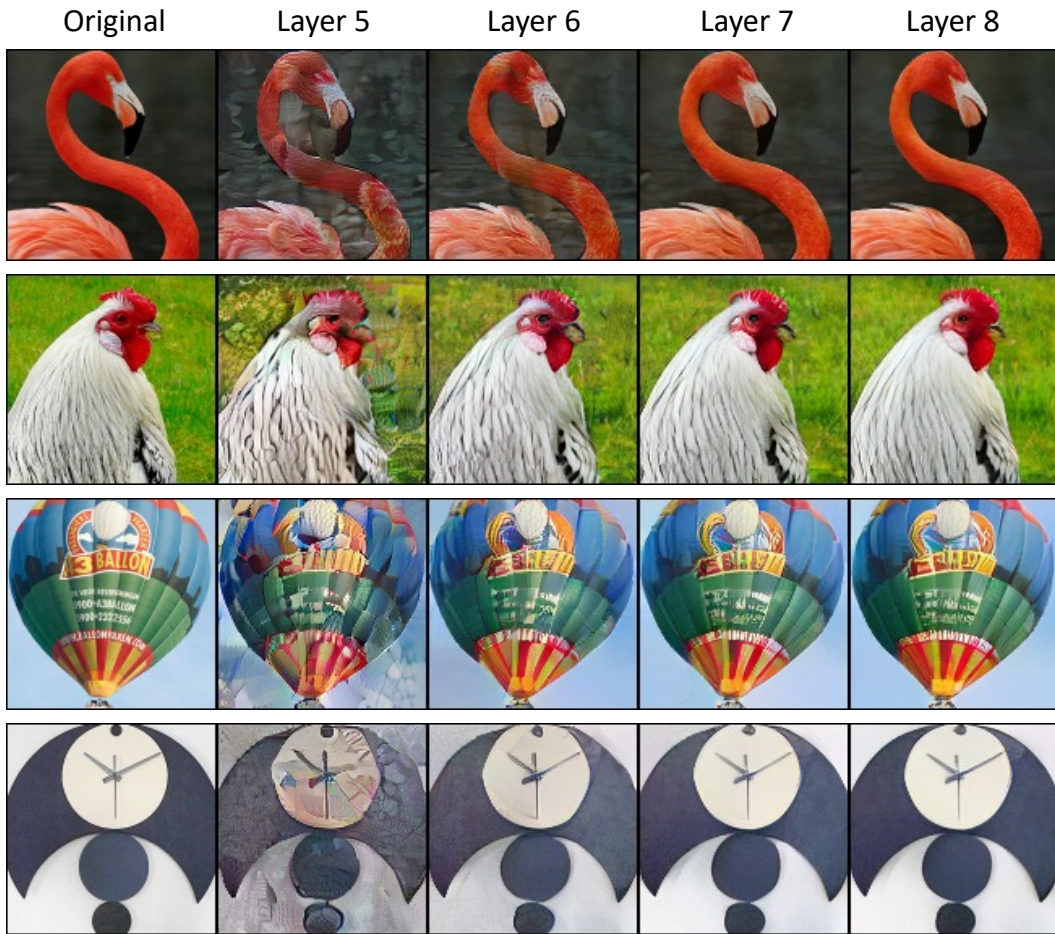


Figure 14. **Examples of coarse-to-fine image reconstruction** by SPAE-8. The top 5 layers reconstruct a noisy image. The appearance details gradually get refined as more token layers are aggregated by the streaming average quantization process.

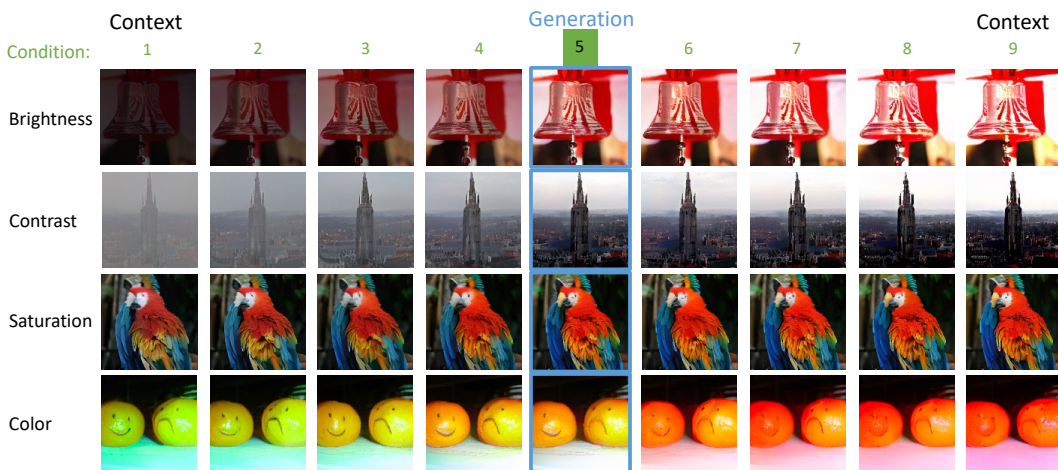


Figure 15. **Examples of conditional image interpolation** of different image transformations.

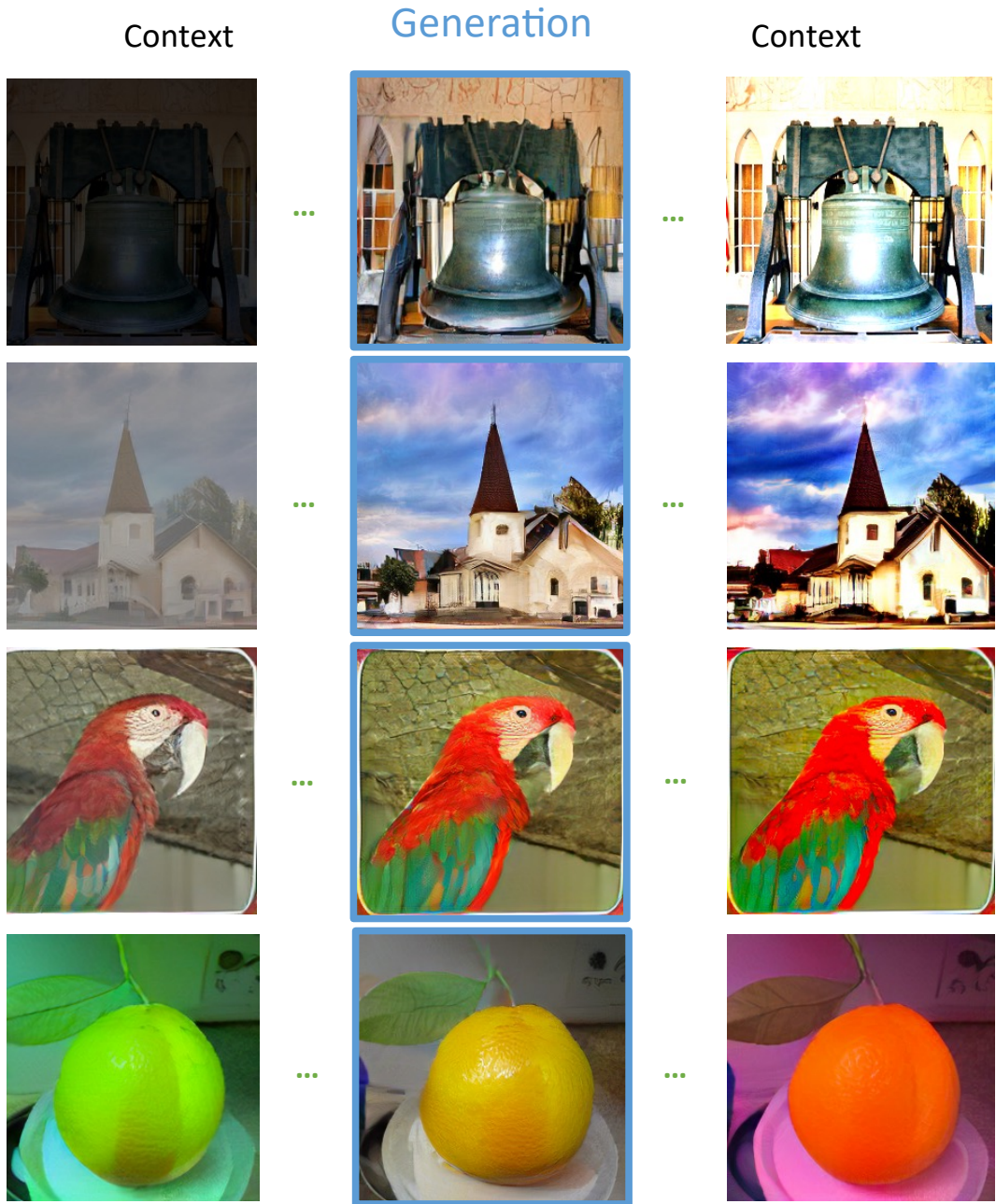
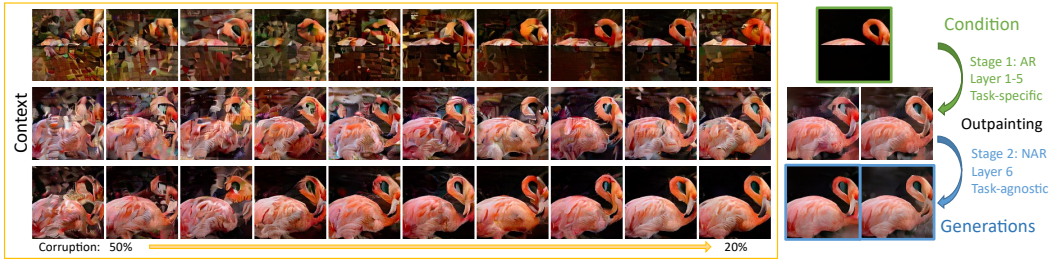


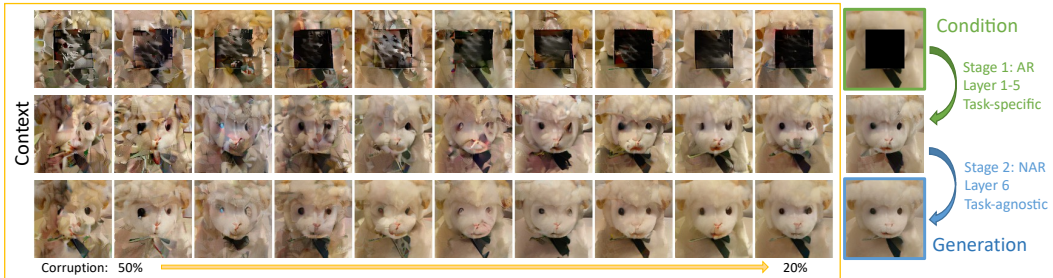
Figure 16. **Examples of conditional image interpolation** at 256x256 resolution. The LLM is provided with eight condition images for the interpolation following the setup in Fig. 15.



(a) Outpainting the bottom half. Two generated images are shown.



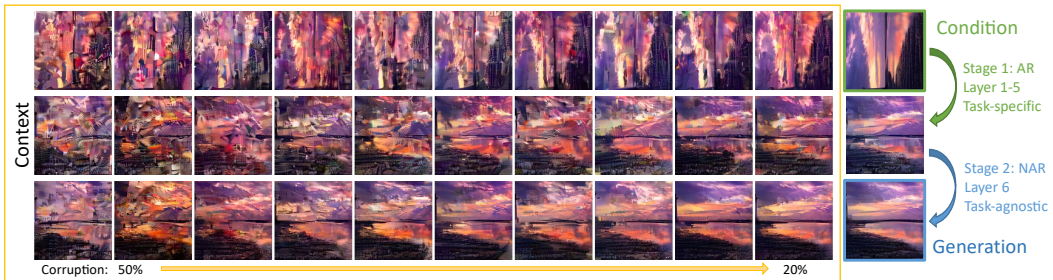
(b) Deblur from a gaussian filter.



(c) Inpainting the center region.



(d) Spatial translation to the right.



(e) Clockwise rotation by 90 degrees.

Figure 17. **Examples of conditional image denoising.** All input samples for the in-context learning are presented for the examples in Figs. 7 and 9. The LLM generates novel images based on the provided context. Multiple different generations can be obtained from the same set of context samples.



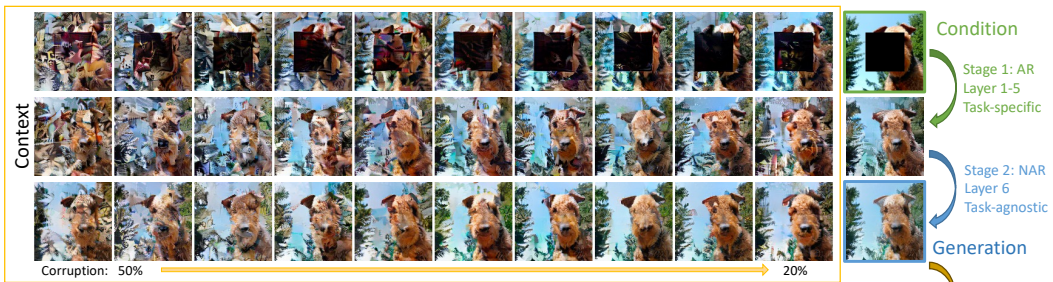


(a) Inpainting the center region.



(b) Outpainting the bottom half.

Figure 18. **More examples of conditional image denoising.** The LLM generates novel images based on the provided context image pairs.



A dog with a long, curly coat of fur.  
 A small dog with a big smile.  
 A small dog with long hair looks up at the camera.

Figure 19. **Examples of multimodal outputs** from the LLM. The LLM generates a novel image with multiple captions based on the provided context.

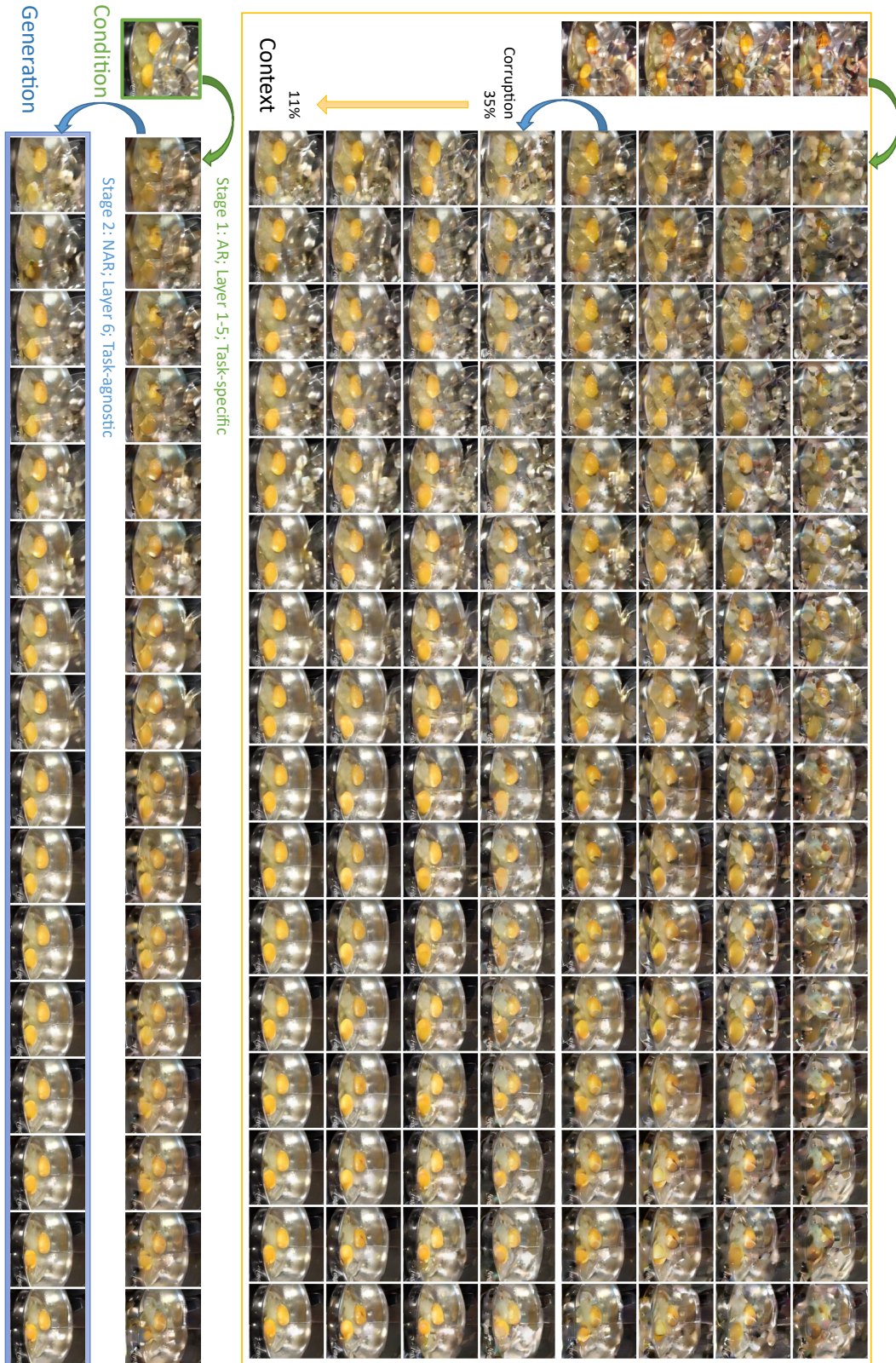


Figure 20. **Examples of image-to-video denoising:** frame prediction. We follow the same two-stage generation procedure as in image-to-image tasks. Due to the sequence length limit, only four samples can be fit into the context. The generated video clip appear visually different from the context samples, especially around the reflections of the bowl.

## References

- [1] Joao Carreira, Eric Noland, Andras Banki-Horvath, Chloe Hillier, and Andrew Zisserman. A short note about Kinetics-600. *arXiv:1808.01340*, 2018. [15](#)
- [2] Huiwen Chang, Han Zhang, Lu Jiang, Ce Liu, and William T Freeman. MaskGIT: Masked generative image transformer. In *CVPR*, 2022. [14](#)
- [3] Jia Deng, Wei Dong, Richard Socher, Li-Jia Li, Kai Li, and Li Fei-Fei. ImageNet: A large-scale hierarchical image database. In *CVPR*, 2009. [18](#)
- [4] Li Deng. The mnist database of handwritten digit images for machine learning research [best of the web]. *IEEE Signal Processing Magazine*, 29(6):141–142, 2012. [15](#)
- [5] Patrick Esser, Robin Rombach, and Bjorn Ommer. Taming transformers for high-resolution image synthesis. In *CVPR*, 2021. [15](#), [19](#)
- [6] Taku Kudo and John Richardson. Sentencepiece: A simple and language independent subword tokenizer and detokenizer for neural text processing. In *EMNLP*, 2018. [17](#)
- [7] Doyup Lee, Chiheon Kim, Saehoon Kim, Minsu Cho, and Wook-Shin Han. Autoregressive image generation using residual quantization. In *CVPR*, 2022. [14](#), [19](#)
- [8] Hao Liu, Wilson Yan, and Pieter Abbeel. Language quantized autoencoders: Towards unsupervised text-image alignment. *arXiv:2302.00902*, 2023. [15](#), [18](#)
- [9] Oriol Vinyals, Charles Blundell, Timothy Lillicrap, Daan Wierstra, et al. Matching networks for one shot learning. In *NeurIPS*, 2016. [15](#), [18](#)
- [10] Lijun Yu, Yong Cheng, Kihyuk Sohn, José Lezama, Han Zhang, Huiwen Chang, Alexander G Hauptmann, Ming-Hsuan Yang, Yuan Hao, Irfan Essa, et al. MAGVIT: Masked generative video transformer. In *CVPR*, 2023. [15](#)
- [11] Neil Zeghidour, Alejandro Luebs, Ahmed Omran, Jan Skoglund, and Marco Tagliasacchi. Soundstream: An end-to-end neural audio codec. *IEEE/ACM Trans. on Audio, Speech, and Language Processing*, 30:495–507, 2021. [14](#)